Supporting Information

Unlocking the Capacity of Mn-based Prussian Blue Cathodes in Capacitive Deionization

Yuhao Lei [1#], Shiyong Wang [1#,*], Gang Wang [1,*], Xiaoyan Shen [2], Lin Zhao [1,2], Xueyang Zhang [1], Shuwen Du [1], Chen Yang [1], Jieshan Qiu [2,*]

[1] School of Environment and Civil Engineering, Research Center for Eco-environmental Engineering, Dongguan University of Technology, Dongguan 523106, Guangdong, PR China

[2] College of Chemical Engineering, Beijing University of Chemical Technology, Beijing 100029, PR China

[#] These authors contributed equally: Yuhao Lei, Shiyong Wang

* Corresponding author. E-mail: wsyongcqu@126.com (SY Wang)

wghy1979@163.com (G Wang)

qiujs@mail.buct.edu.cn (JS Qiu)

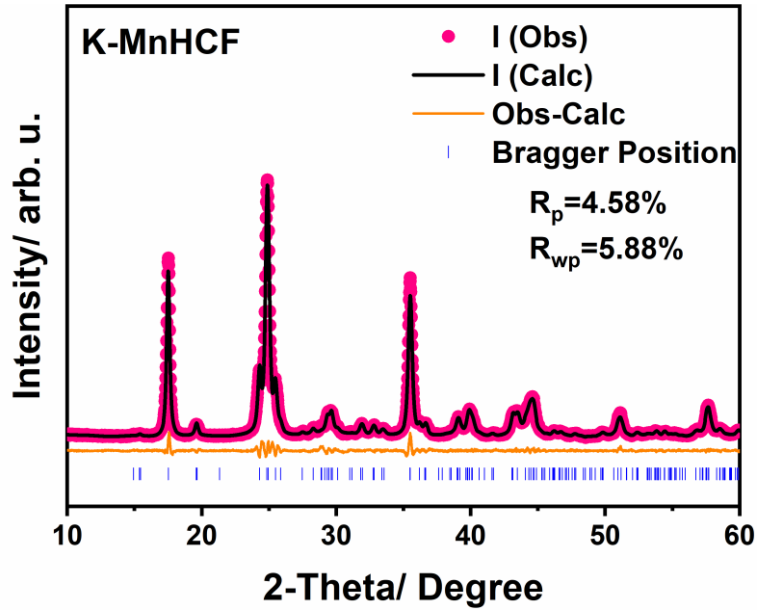

Supplementary Fig. 1 The Rietveld refinement of XRD patterns of K-MnHCF. Source data are provided as a Source Data file.

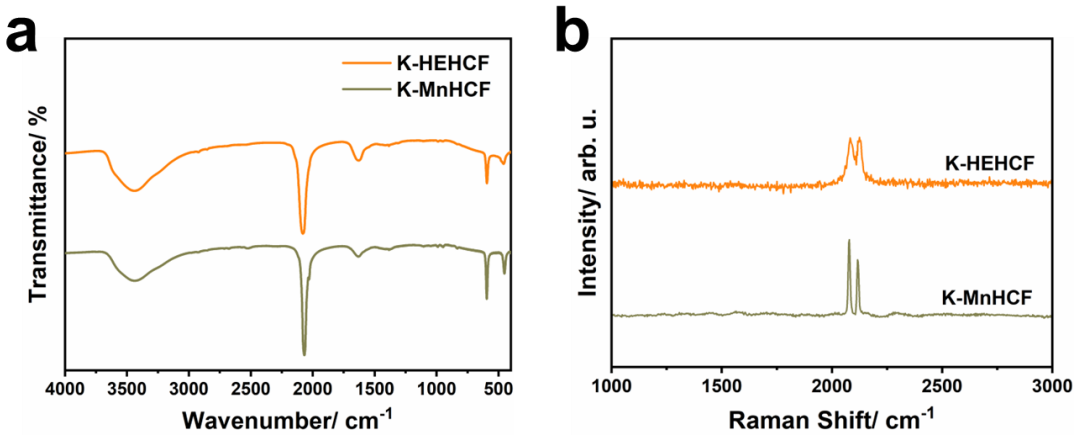

Supplementary Fig. 2 Structural Characterization of K-Based PBAs. (a) FT-IR and (b) Raman spectra of K-HEHCF and K-MnHCF. Source data are provided as a Source Data file.

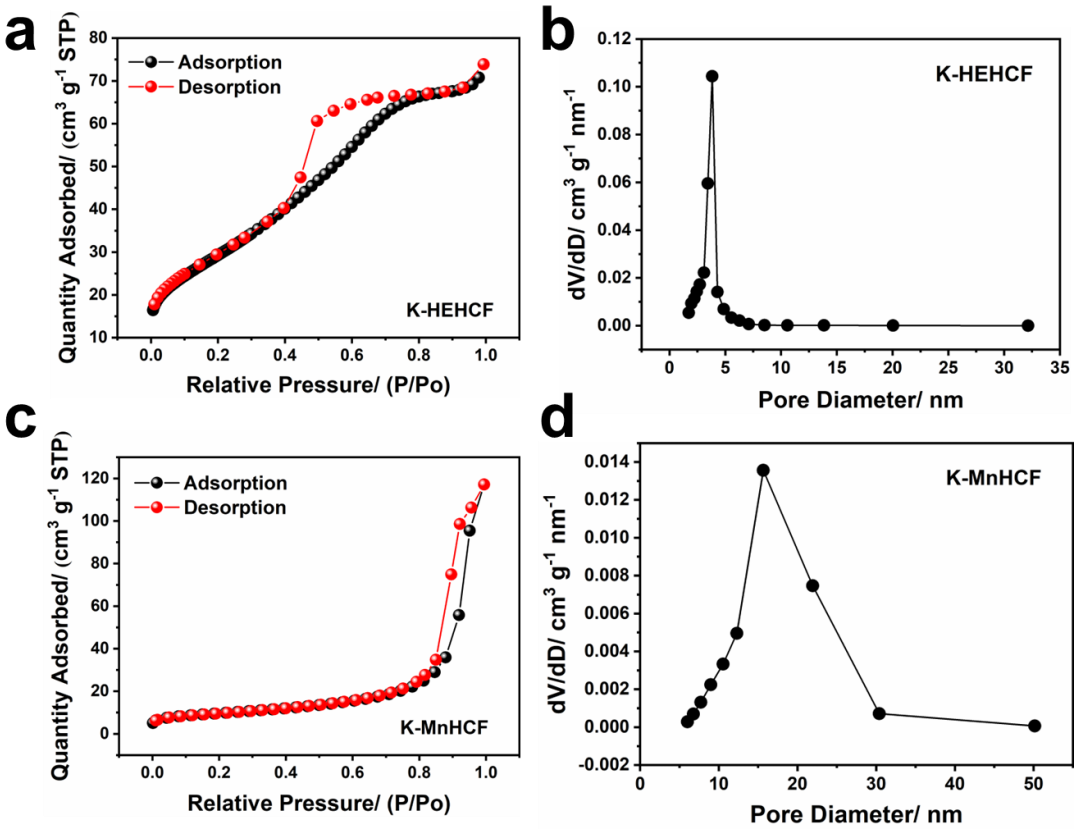

Supplementary Fig. 3 N_2 adsorption-desorption isotherms and pore size distributions. (a, b) K-HEHCF. (c, d) K-MnHCF. Source data are provided as a Source Data file.

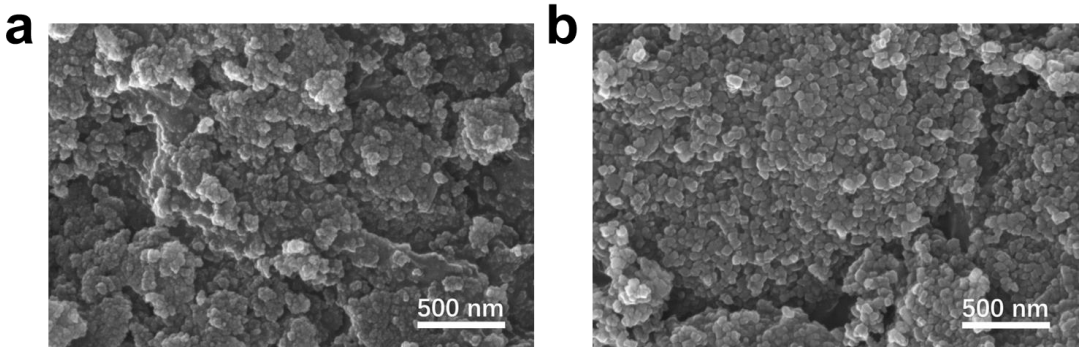

Supplementary Fig. 4 SEM images of (a) K-HEHCF and (b) K-MnHCF.

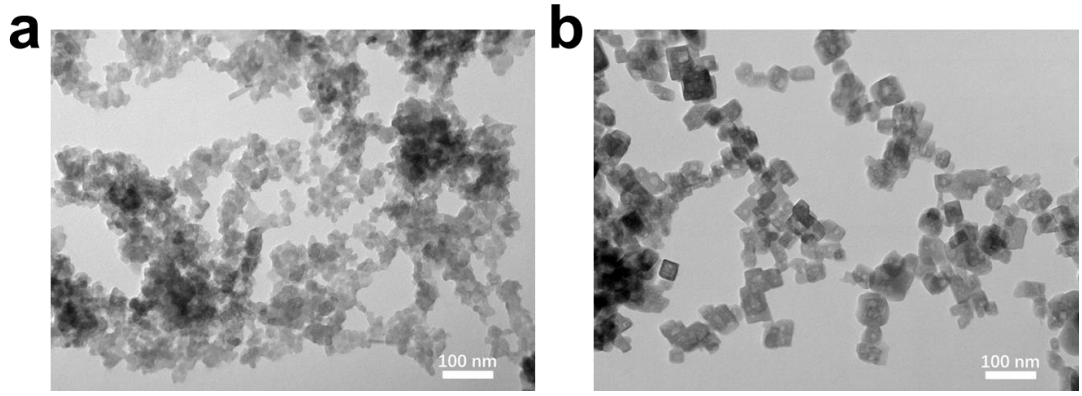

Supplementary Fig. 5 TEM images of (a) K-HEHCF and (b) K-MnHCF.

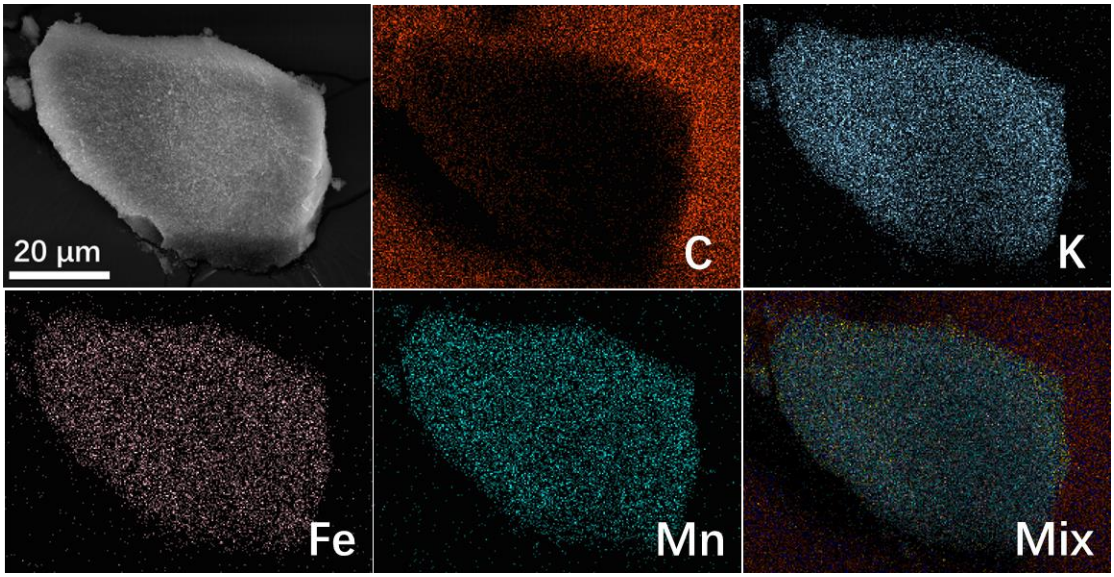

Supplementary Fig. 6 SEM image and the corresponding elemental maps of K-MnHCF.

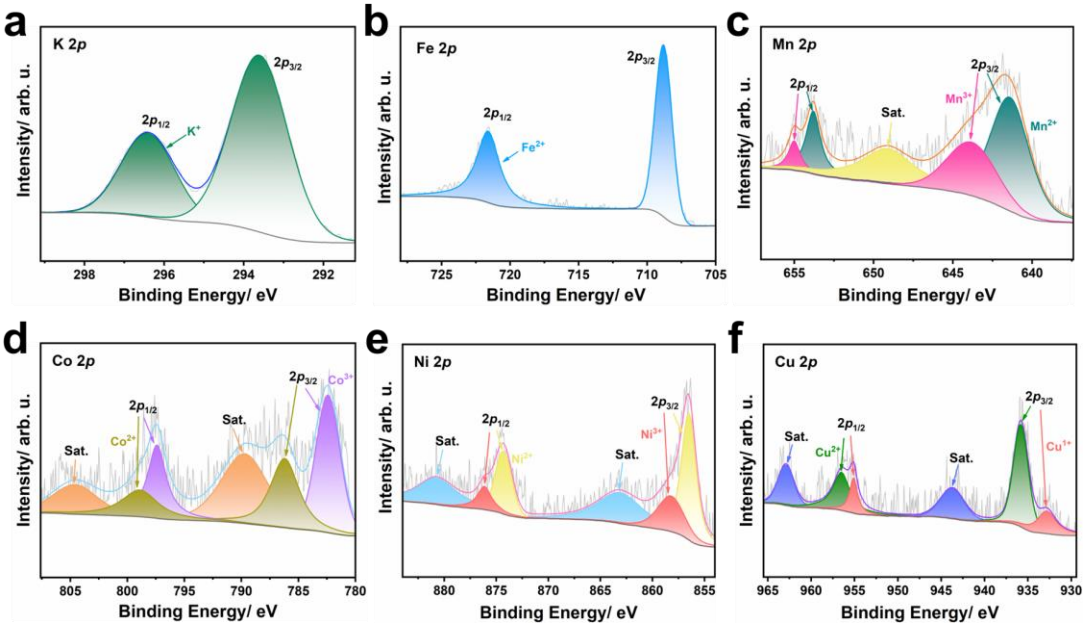

Supplementary Fig. 7 High-resolution XPS spectra of (a) K 2*p*, (b) Fe 2*p*, (c) Mn 2*p*, (d) Co 2*p*, (e) Ni 2*p* and (f) Cu 2*p* for K-HEHCF. Source data are provided as a Source Data file.

The K 2*p* spectrum displays two peaks at the binding energies of 293.6 and 296.4 eV[1] (Fig. 7a). In the Fe 2*p* spectrum, the typical peaks at 708.8 and 721.6 eV are attributed to Fe $2p_{3/2}$ and Fe $2p_{1/2}$ of Fe^{2+2} (Fig. 7b). In the Mn 2*p* spectrum, the peaks at 643.8 and 655 eV are attributed to Mn $2p_{3/2}$ and Mn $2p_{1/2}$ of Mn^{3+}, and 641.4 and 653.8 eV are attributed to Mn^{2+} of Mn $2p_{3/2}$ and Mn $2p_{1/2}$[3] (Fig. 7c). For Co 2*p* spectrum, the peaks at 786.2 eV (Co $2p_{3/2}$) and 798.9 eV (Co $2p_{1/2}$) belong to Co^{2+}, and the peaks at 782.4 (Co $2p_{3/2}$) and 797.4 eV (Co $2p_{1/2}$) belong to Co^{3+4} (Fig. 7d). For Ni 2*p* spectrum, 856.5 and 874.3 eV are Ni^{2+} and 858.2 and 876.1 eV are Ni^{3+}, indicating the coexistence of divalent and trivalent Ni[6] (Fig. 7e). For Cu 2*p* spectrum, 935.8 and 956.5 eV are Cu^{2+} and 933.1 and 955.1 eV are Cu^{1+5} (Fig. 7f).

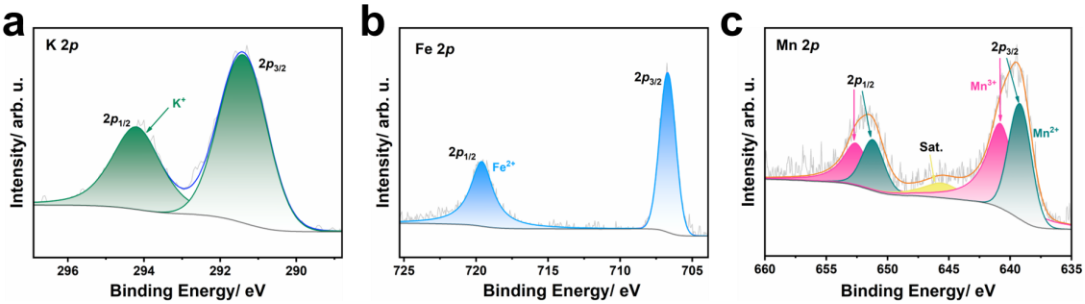

Supplementary Fig. 8 High-resolution XPS spectra of (a) K 2*p*, (b) Fe 2*p* and (c) Mn 2*p* for K-MnHCF. Source data are provided as a Source Data file.

The XPS analysis of K-MnHCF revealed that the spectral results for Fe, Mn and K were similar to those of K-HEHCF.

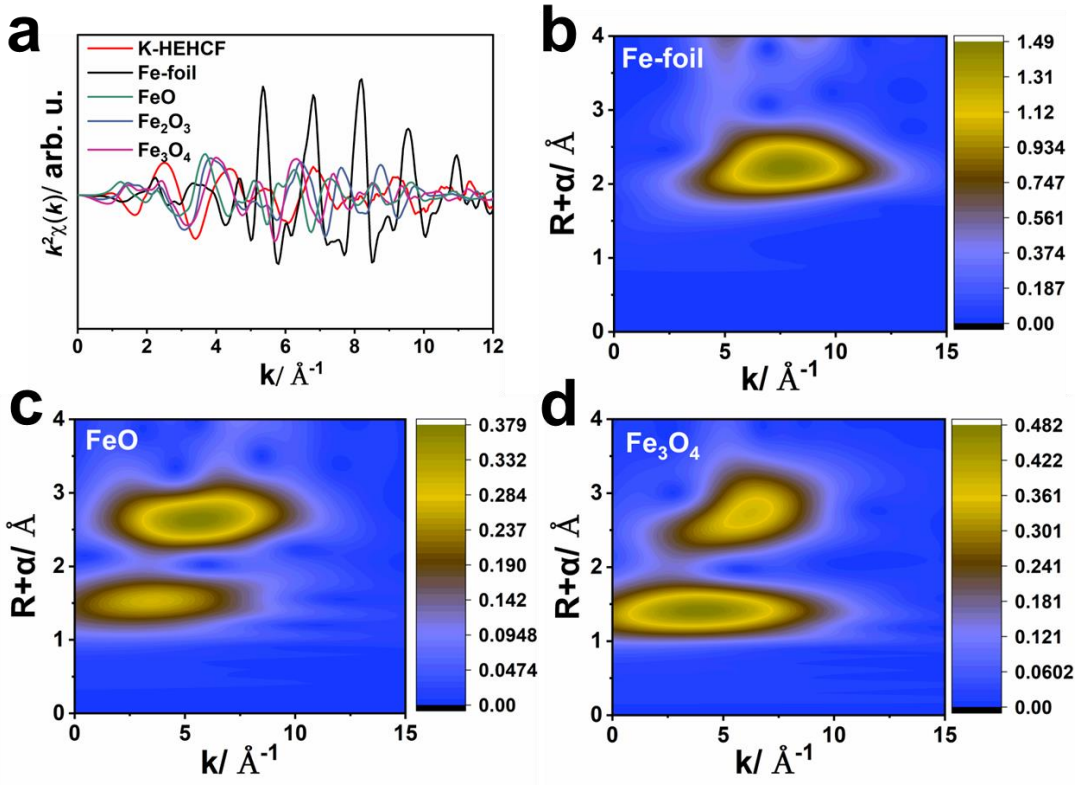

Supplementary Fig. 9 EXAFS Analysis of Fe in K-HEHCF. (a) Fe K-edge EXAFS oscillation functions $k^2\chi(k)$ of K-HEHCF, Fe-foil, FeO and Fe_3O_4. (b-d) Wavelet transformation of EXAFS spectra of Fe-foil, FeO and Fe_3O_4. Source data are provided as a Source Data file.

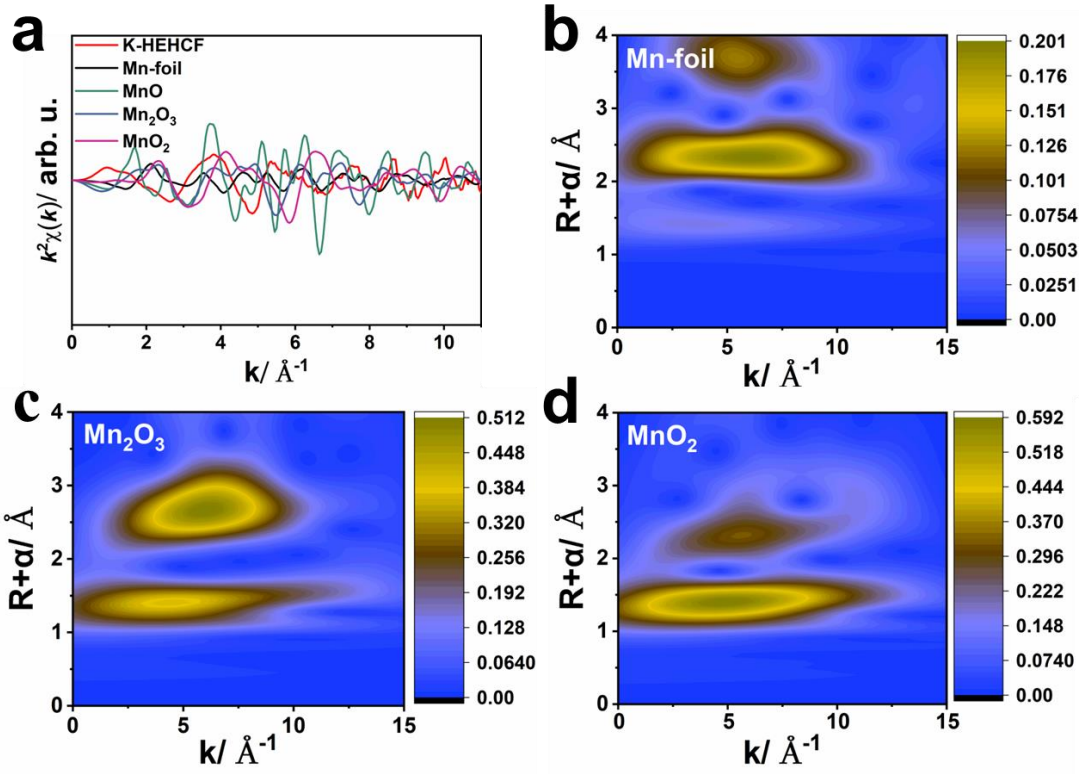

Supplementary Fig. 10 EXAFS Analysis of Mn in K-HEHCF. (a) Mn K-edge EXAFS oscillation functions $k^2\chi(k)$ of K-HEHCF, Mn-foil, MnO, Mn_2O_3 and MnO_2. (b-d) Wavelet transformation of EXAFS spectra of Mn-foil, Mn_2O_3 and MnO_2. Source data are provided as a Source Data file.

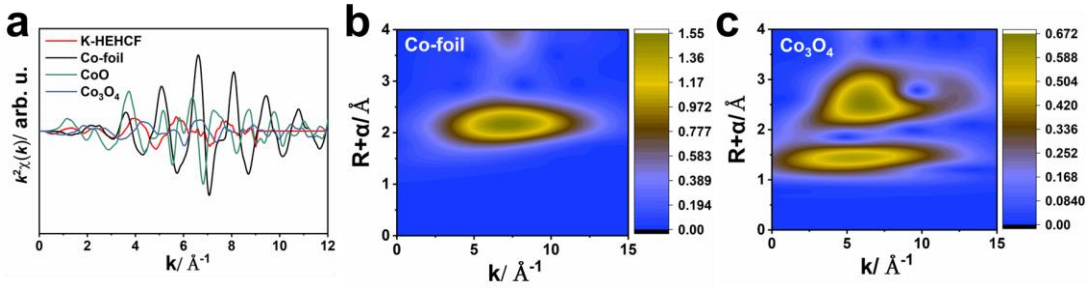

Supplementary Fig. 11 EXAFS Analysis of Co in K-HEHCF. (a) Co K-edge EXAFS oscillation functions $k^2\chi(k)$ of K-HEHCF, Co-foil, CoO, Co_3O_4. (b, c) Wavelet transformation of EXAFS spectra of Co-foil and Co_3O_4. Source data are provided as a Source Data file.

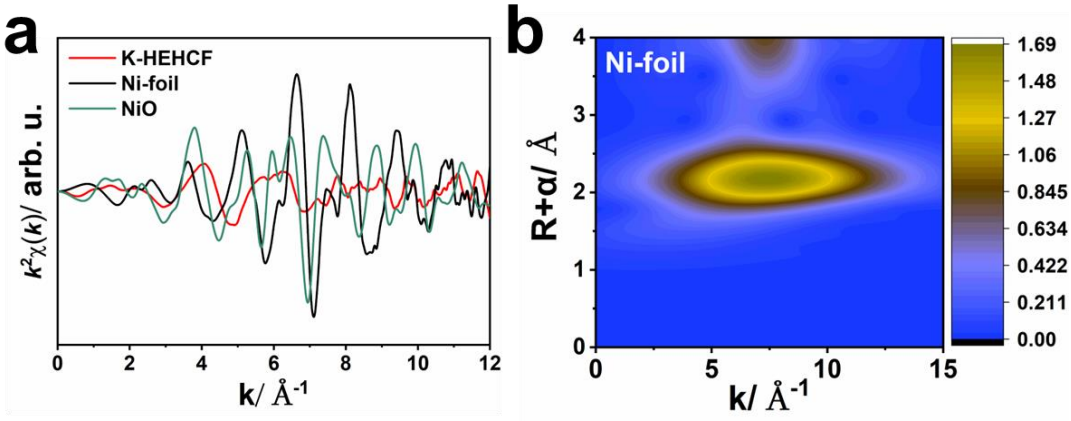

Supplementary Fig. 12 EXAFS Analysis of Ni in K-HEHCF. (a) Ni K-edge EXAFS oscillation functions $k^2\chi(k)$ of K-HEHCF, Ni-foil and NiO. (b) Wavelet transformation of EXAFS spectra of Ni-foil. Source data are provided as a Source Data file.

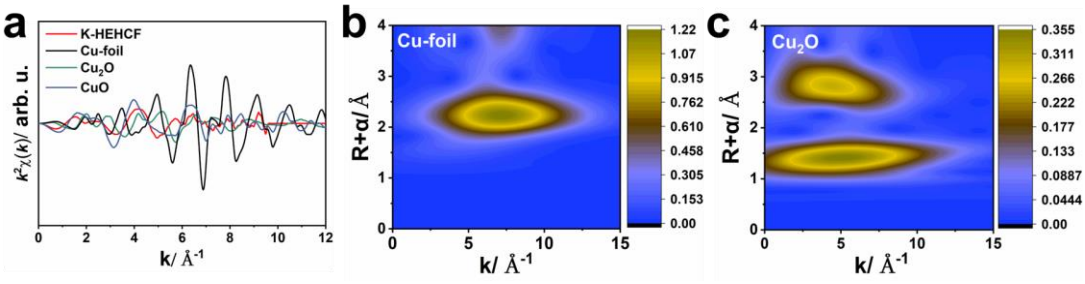

Supplementary Fig. 13 EXAFS Analysis of Cu in K-HEHCF. (a) Cu K-edge EXAFS oscillation functions $k^2\chi(k)$ of K-HEHCF, Cu-foil, Cu_2O, CuO. (b, c) Wavelet transformation of EXAFS spectra of Cu-foil and Cu_2O. Source data are provided as a Source Data file.

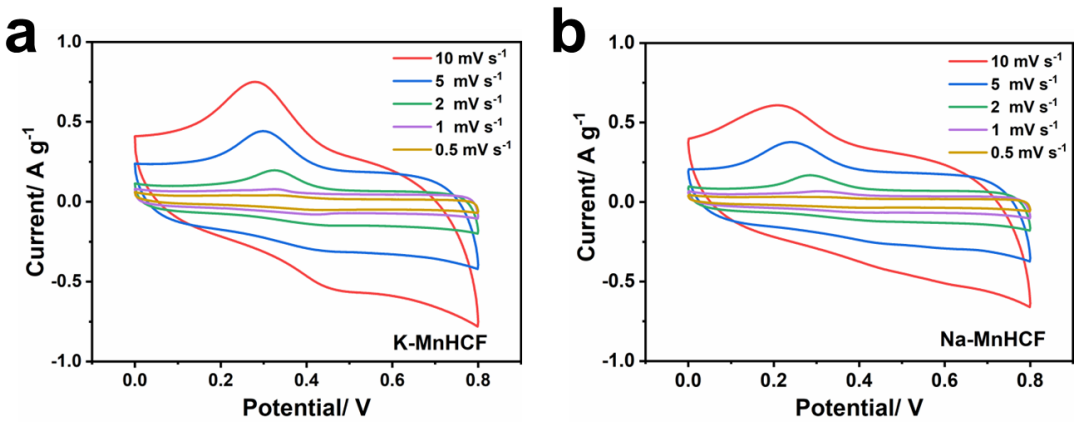

Supplementary Fig. 14 CV curves of (a) K-MnHCF and (b) Na-MnHCF at different scan rates. Source data are provided as a Source Data file.

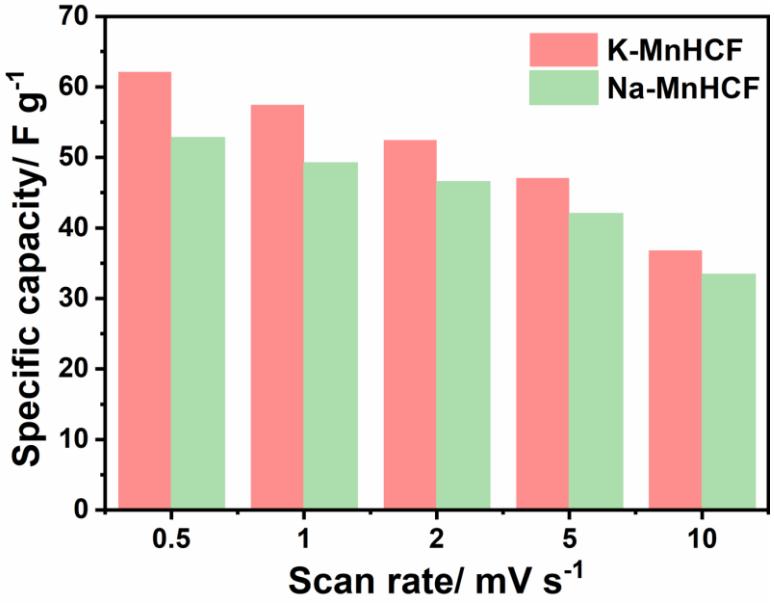

Supplementary Fig. 15 Comparison of Specific capacitance of (a) K-MnHCF and (b) Na-MnHCF. Source data are provided as a Source Data file.

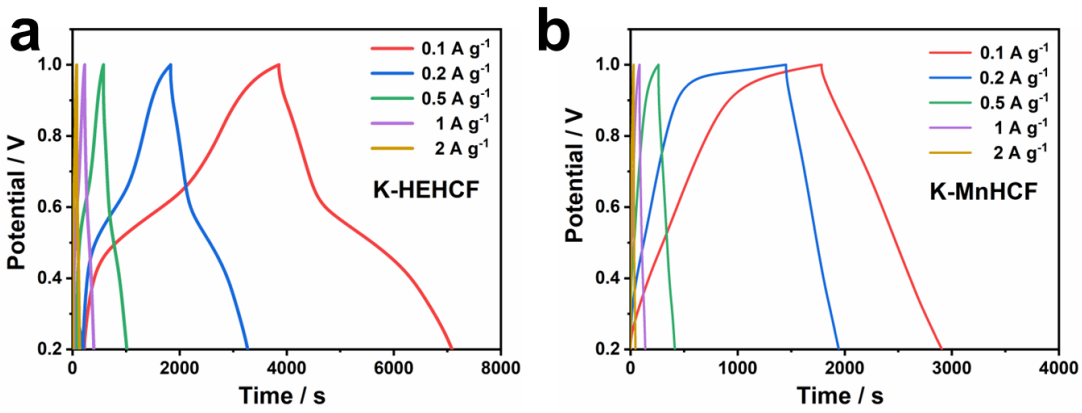

Supplementary Fig. 16 GCD curves at different scan rates of (a) K-HEHCF and (b) K-MnHCF. Source data are provided as a Source Data file.

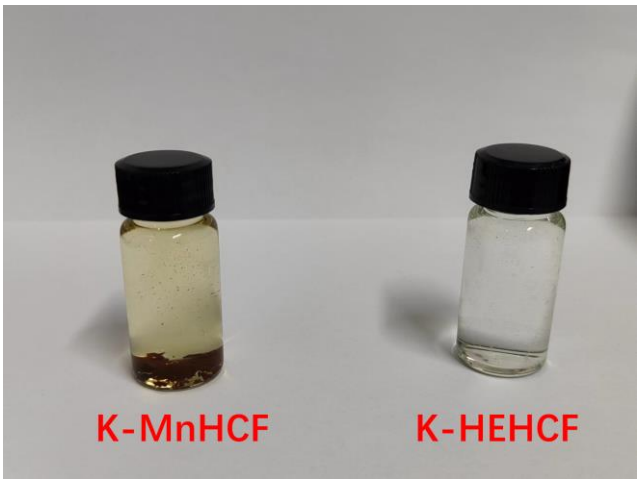

Supplementary Fig. 17 Comparison of two electrolyte colors after 1000 cycles.

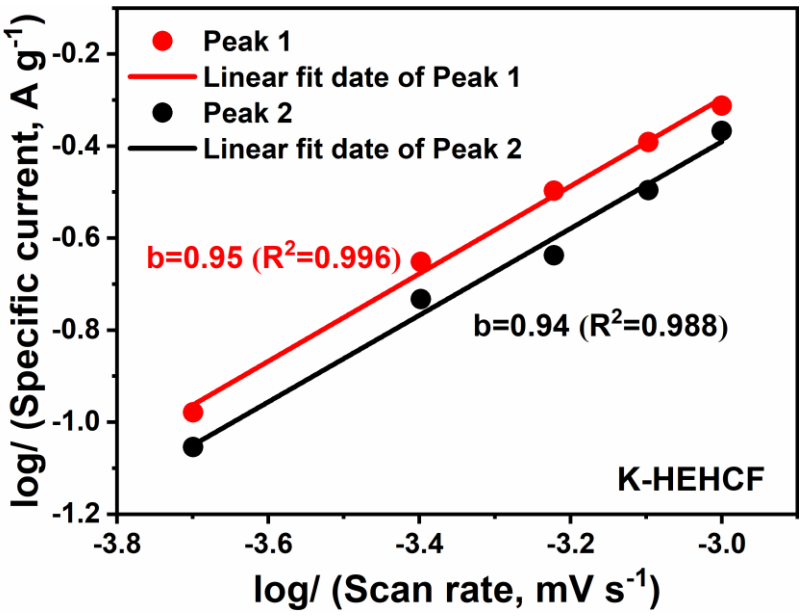

Supplementary Fig. 18 Linear correlation between the logarithmic peak current and sweep rate of K-HEHCF. Source data are provided as a Source Data file.

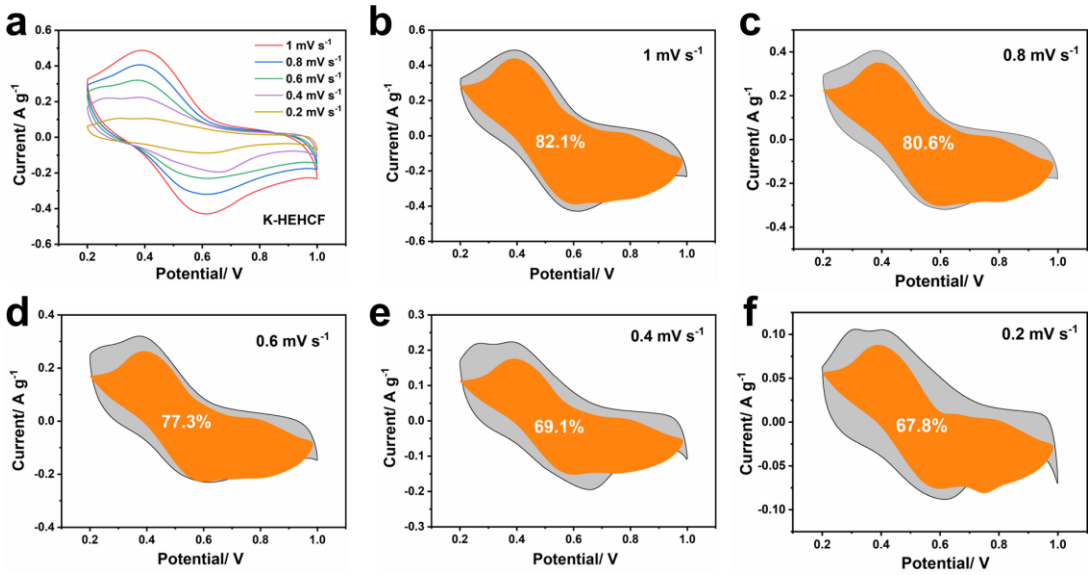

Supplementary Fig. 19 The contribution of capacitive-controlled (color) and diffusion-controlled process (grey) of K-HEHCF at different scan rates. (a) CV curves of K-HEHCF at scan rates ranging from 0.2-1 mV s^{-1}. (b–f) Quantifies the capacitance-controlled portion at different voltages, with percentages indicating the specific proportions. Source data are provided as a Source Data file.

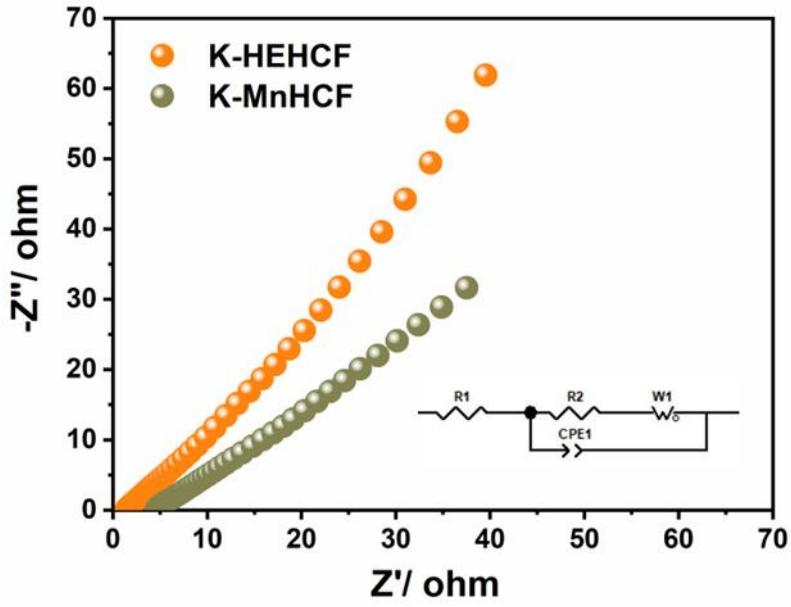

Supplementary Fig. 20 Nyquist plots of K-HEHCF and K-MnHCF (The inserted image is a fitted circuit diagram). Source data are provided as a Source Data file.

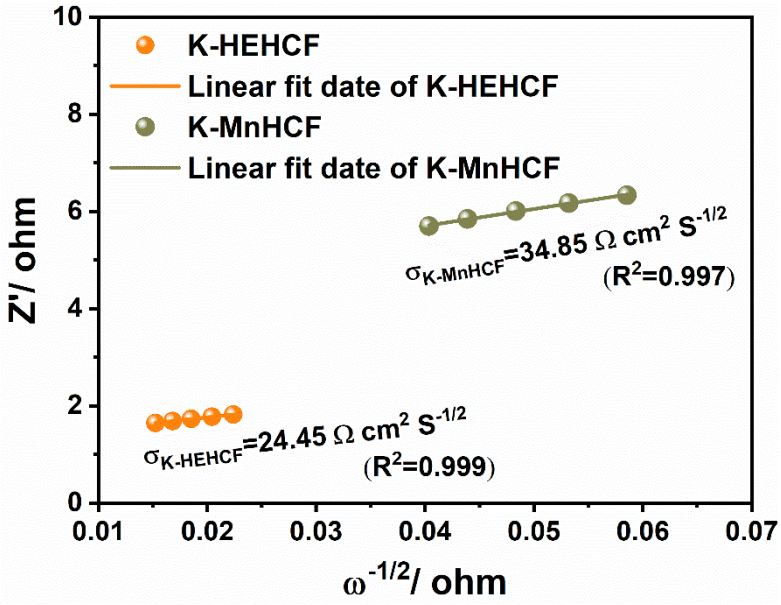

Supplementary Fig. 21 Fitting results for Z` and $\omega^{-1/2}$ in the low frequency range.

Source data are provided as a Source Data file.

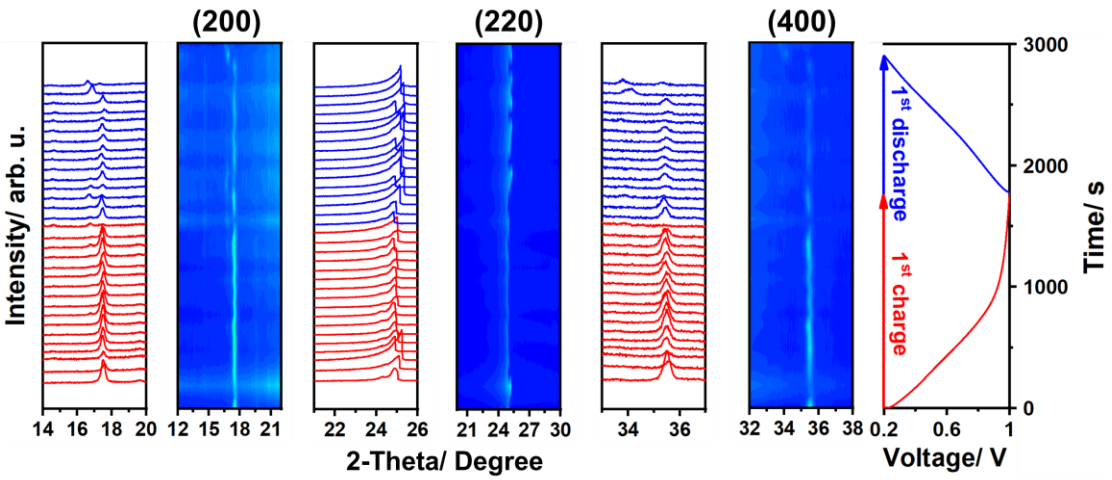

Supplementary Fig. 22 The ex situ XRD pattern of K-MnHCF during the first cycle and corresponding charge/discharge curves. Source data are provided as a Source Data file.

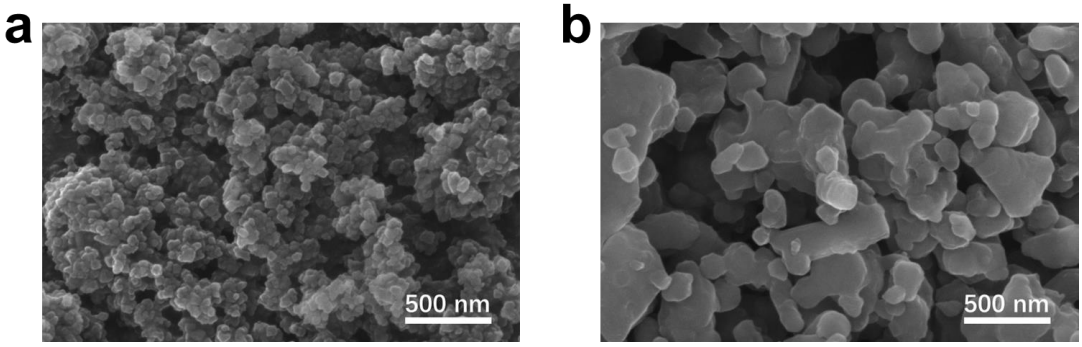

Supplementary Fig. 23 SEM images of (a) Na-HEHCF and (b) Na-MnHCF.

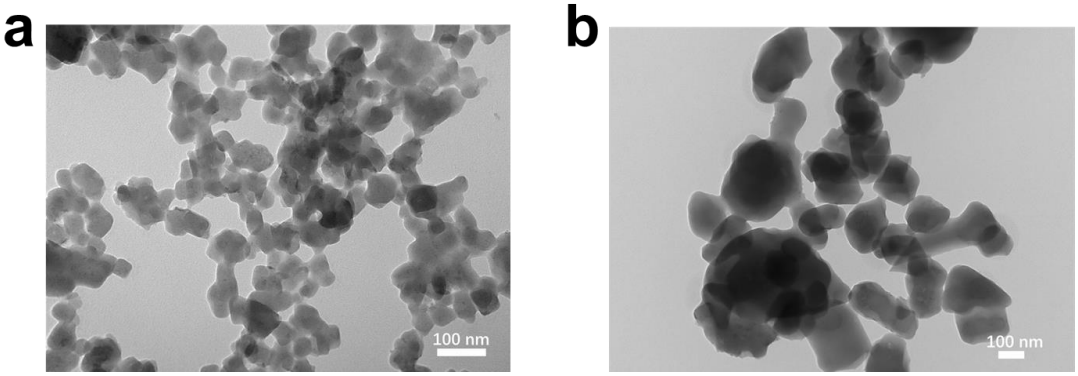

Supplementary Fig. 24 TEM images of (a) Na-HEHCF and (b) Na-MnHCF.

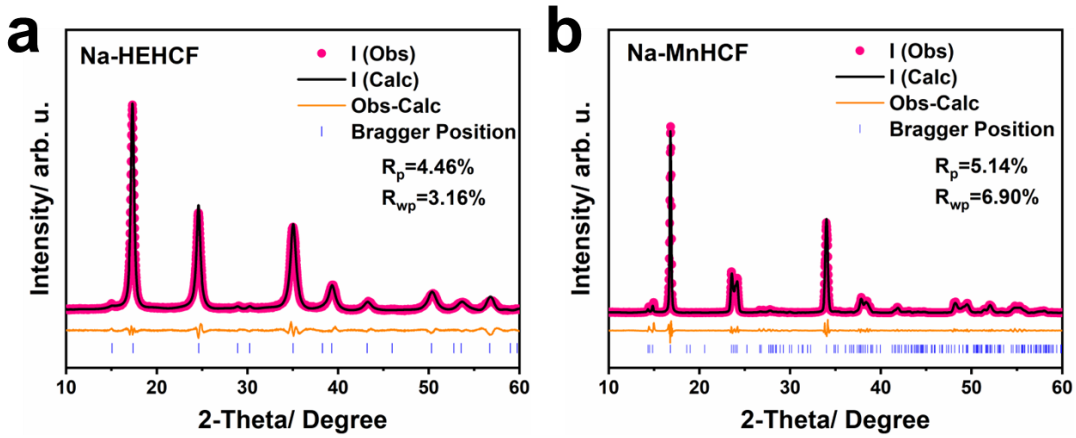

Supplementary Fig. 25 XRD patterns and corresponding Rietveld refinement plots of (a) Na-HEHCF and (b) Na-MnHCF. Source data are provided as a Source Data file.

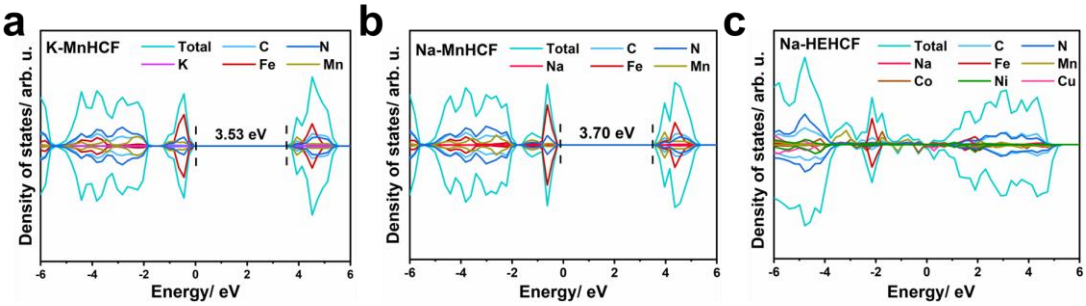

Supplementary Fig. 26 Density of states of (a) K-MnHCF, (b) Na-MnHCF, (c) Na-HEHCF. Source data are provided as a Source Data file.

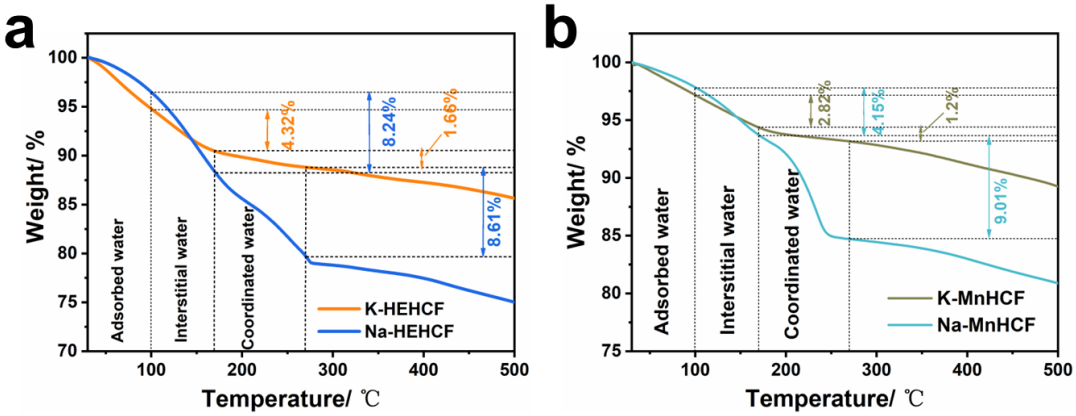

Supplementary Fig. 27 TGA curves of (a) HEHCFs and (b) MnHCFs. Source data are provided as a Source Data file.

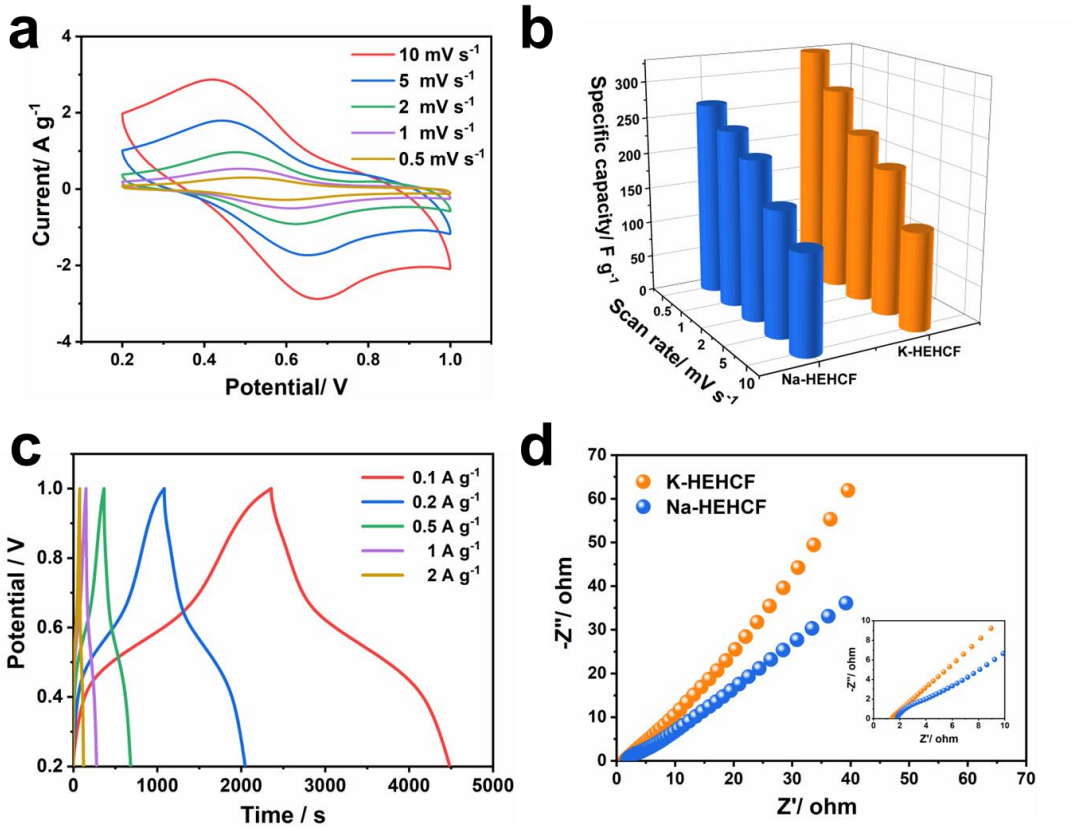

Supplementary Fig. 28 Comparison of the Electrochemical Performance of HEHCFs. (a) CV curves of Na-HEHCF at different scan rates. (b) Comparison of Specific capacitance. (c) GCD curves at different scan rates. (d) Nyquist plots of K-HEHCF and Na-HEHCF (The inserted image is a magnified view of the high frequency region). Source data are provided as a Source Data file.

As the scan rate increases, the peak current gradually increases, while the shape of the CV curve for Na-HEHCF remains unchanged throughout this process (Fig. 28a). The specific capacitance values calculated from the CV curves indicate that K-HEHCF exhibits superior charge storage performance compared to Na-HEHCF at different scan rates (Fig. 28b). Fig. 28c shows the GCD curve of Na-HEHCF. By comparison, it can be seen that the discharge time at various current densities is also inferior to that of K-HEHCF. Additionally, as indicated by the comparison of EIS curves, K-HEHCF

exhibits a larger slope compared to Na-HEHCF, suggesting faster ion diffusion kinetics (Fig. 28d). In summary, the electrochemical performance of K-HEHCF is clearly superior to that of Na-HEHCF.

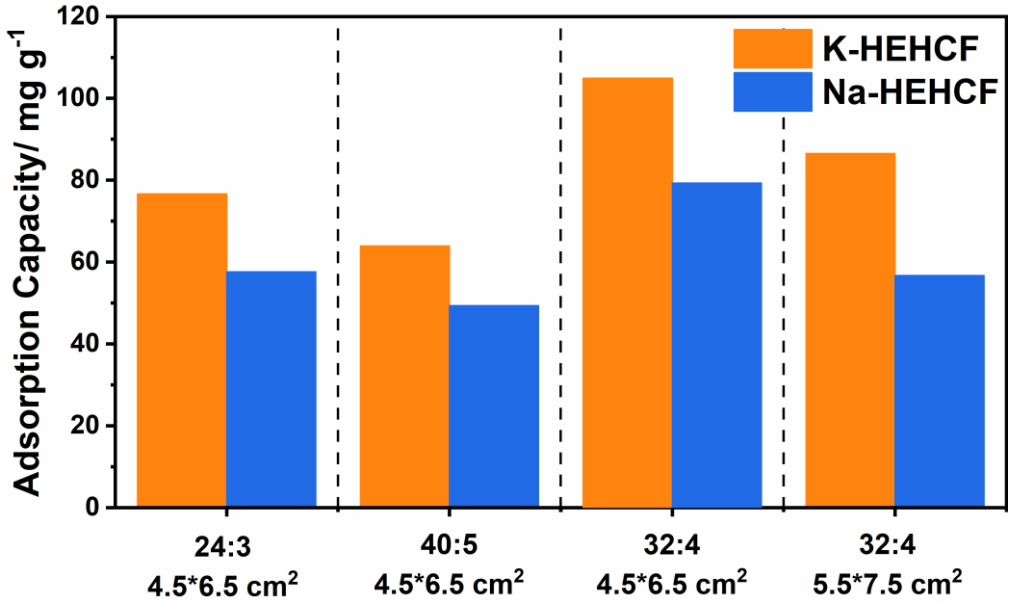

Supplementary Fig. 29 The adsorption capacity of K-HEHCF and Na-HEHCF at various conditions with 500 mg L^{-1} NaCl solution. Source data are provided as a Source Data file.

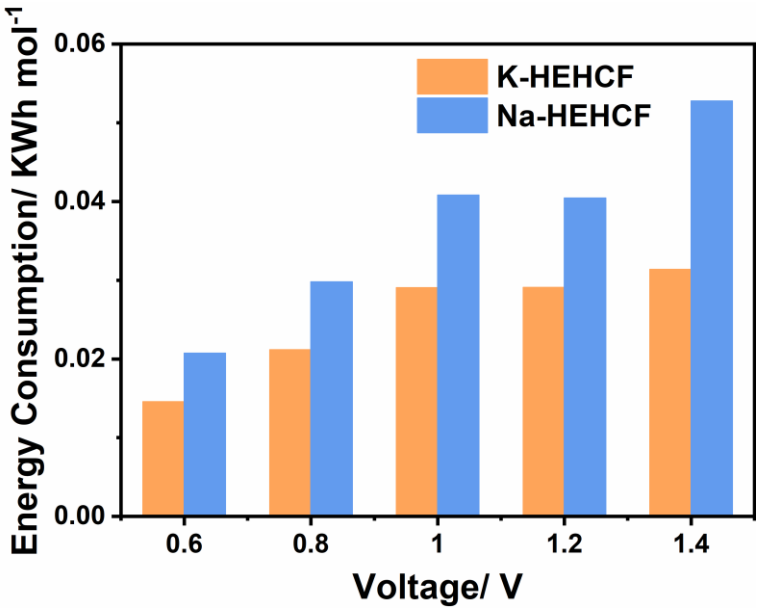

Supplementary Fig. 30 The energy consumption of K-HEHCF and Na-HEHCF at various voltage with 500 mg L^{-1} NaCl solution. Source data are provided as a Source Data file.

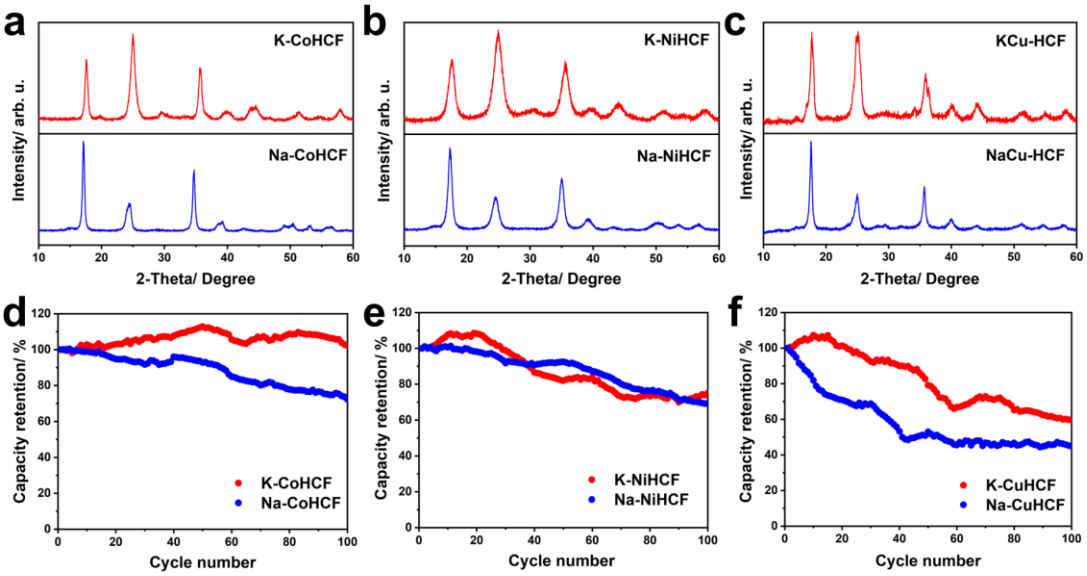

Supplementary Fig. 31 XRD patterns and capacity retention of other single metal-centered PBAs at 1 V. Source data are provided as a Source Data file.

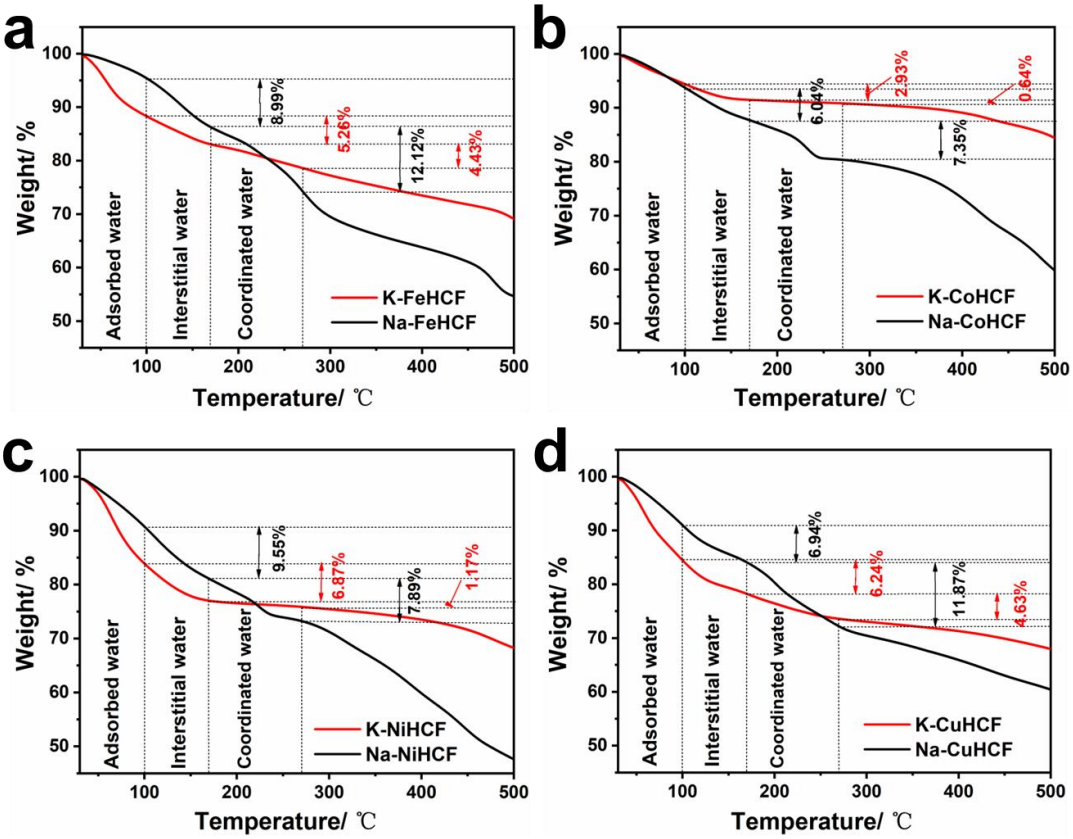

Supplementary Fig. 32 TGA curves of (a) FeHCFs, (b) CoHCFs, (c) NiHCFs and (d) CuHCFs. Source data are provided as a Source Data file.

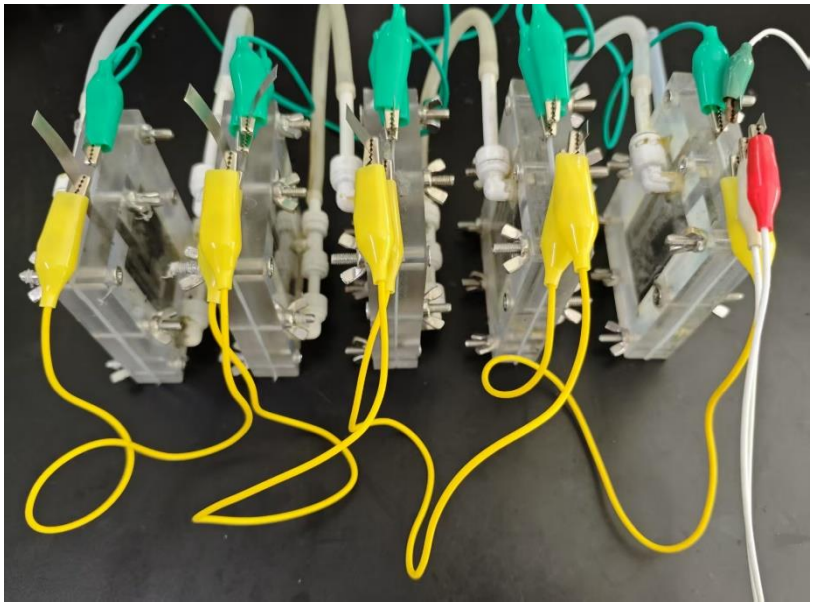

Supplementary Fig. 33 HCDI tandem system consisting of five processing units.

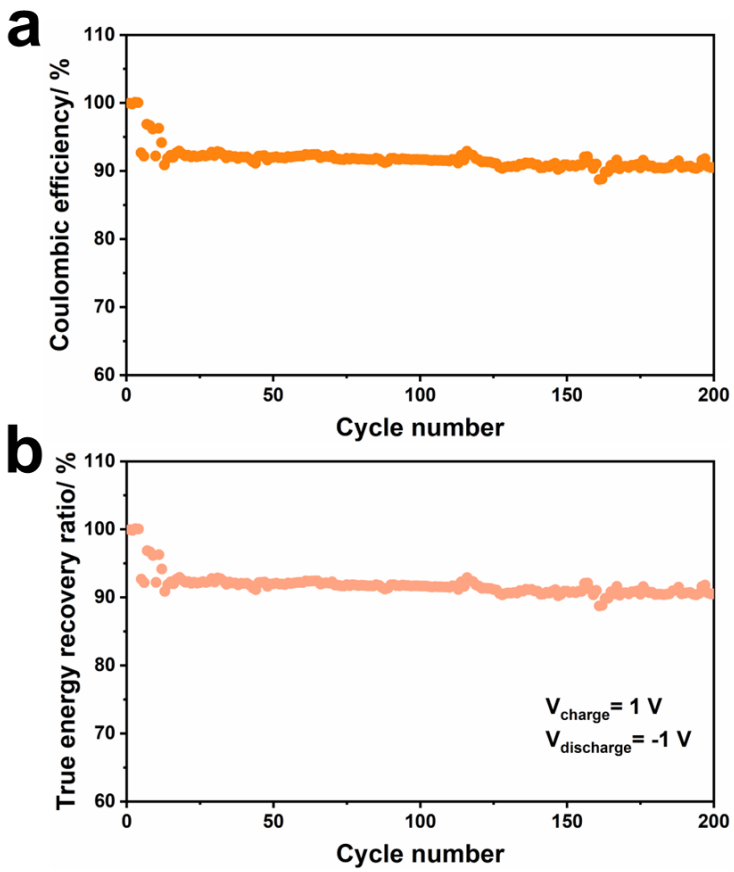

Supplementary Fig. 34 (a) Coulombic efficiency and (b) true energy recovery ratio during CDI cycles. Source data are provided as a Source Data file.

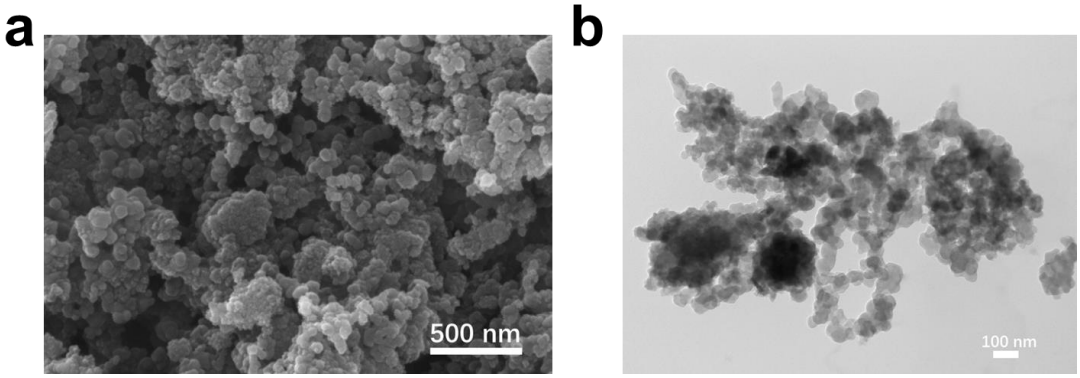

Supplementary Fig. 35 (a) SEM and (b) TEM images after 200 cycling of K-HEHCF.

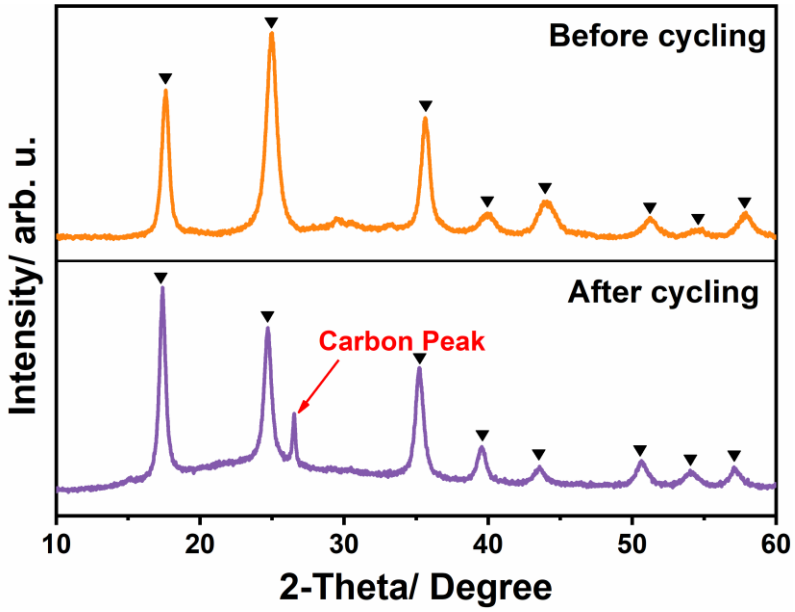

Supplementary Fig. 36 XRD patterns before and after 200 cycling of K-HEHCF.

Source data are provided as a Source Data file.

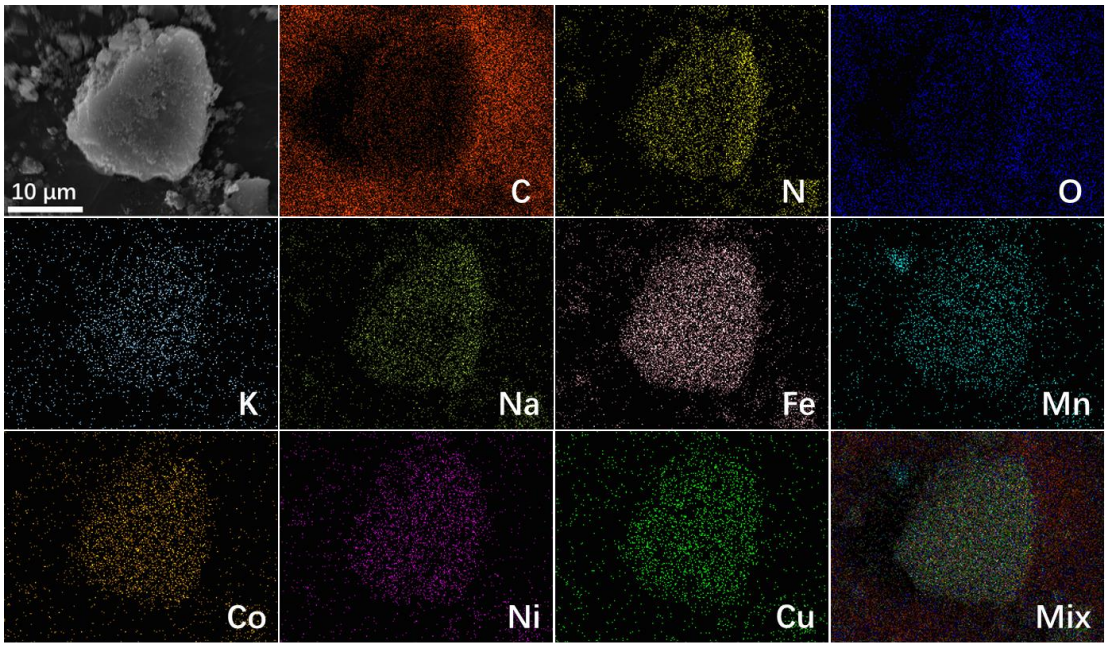

Supplementary Fig. 37 SEM image and the corresponding elemental maps of K-HEHCF after 200 cycling.

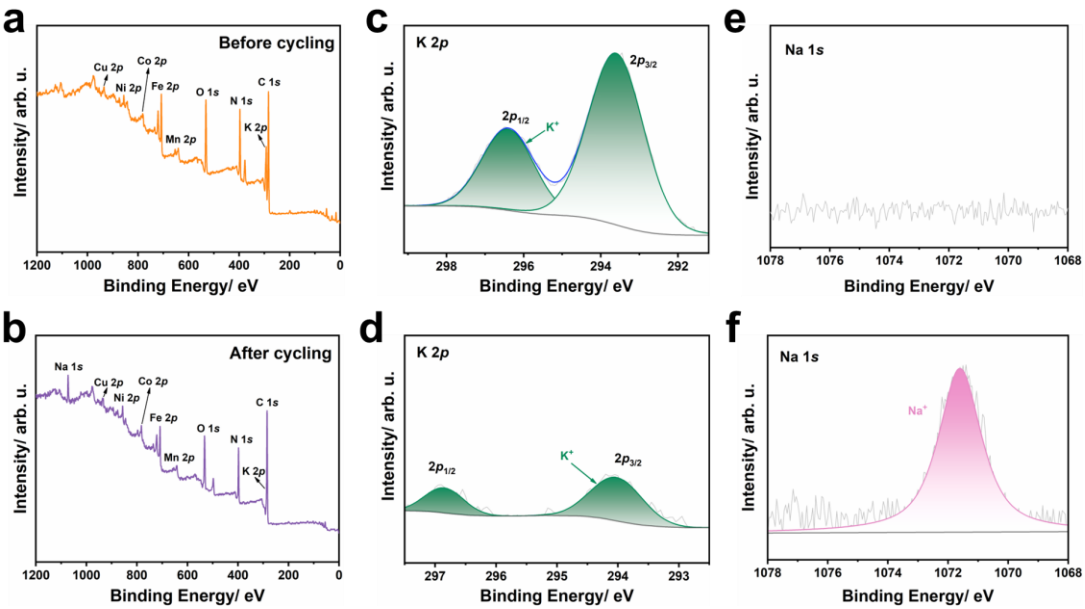

Supplementary Fig. 38 (a, b) XPS survey spectra, (c, d) K 2*p* and (e, f) Na 1*s* spectra of K-HEHCF before and after 200 cycling. Source data are provided as a Source Data file.

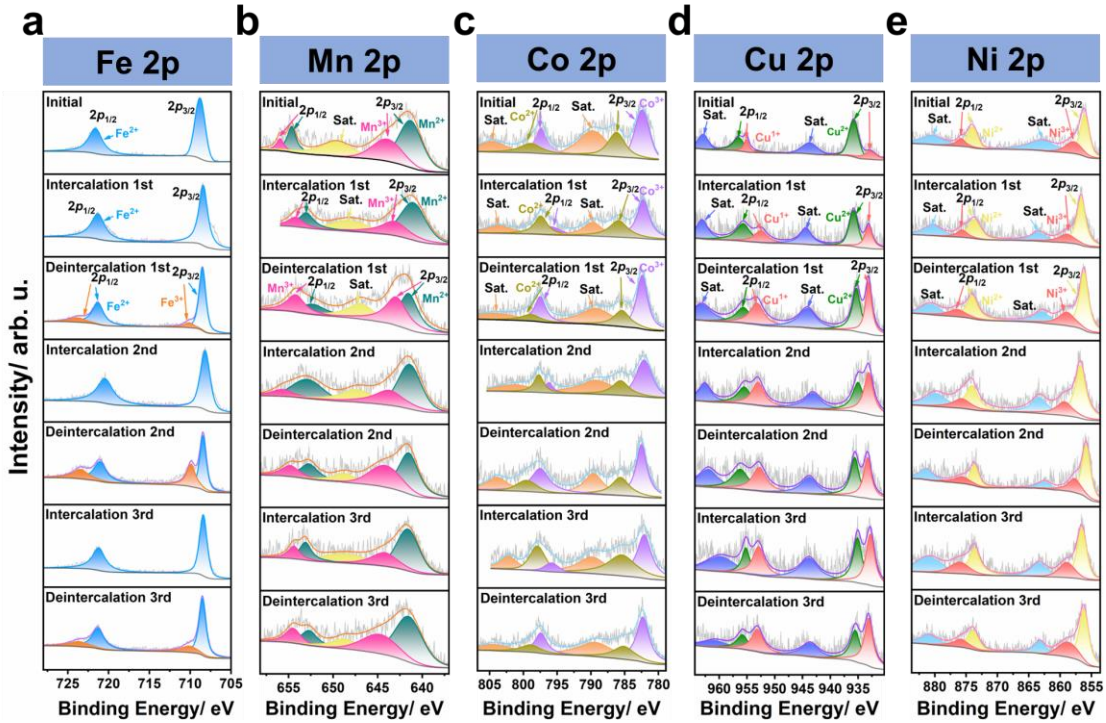

Supplementary Fig. 39 Ex situ XPS analysis of metal component in K-HEHCF electrode at different CDI stages. Source data are provided as a Source Data file.

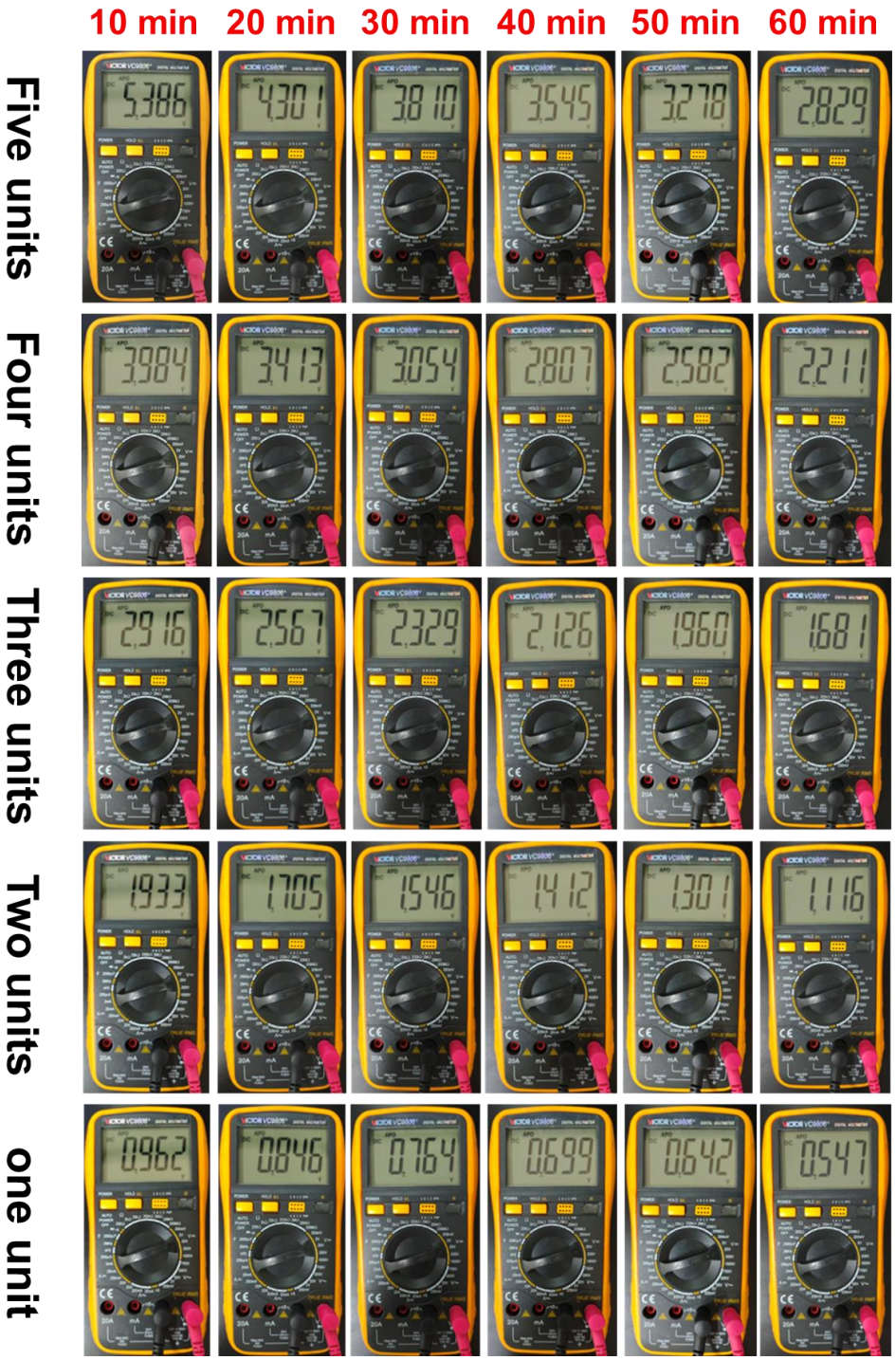

Supplementary Fig. 40 Open-circuit voltage of PBAs/AC CDI cells over time at different numbers of units.

Supplementary Table 1 ICP-OES results of element ratios for K-HEHCF and Na-HEHCF.

Element	K	Fe	Mn	Co	Ni	Cu
Mole ratios	2.07	0.94	0.21	0.2	0.22	0.2

Element	Na	Fe	Mn	Co	Ni	Cu
Mole ratios	3.02	0.75	0.24	0.22	0.18	0.19

Calculate the configuration entropy of K-HEHCF and Na-HEHCF according to equations 1-2 of the Methods.

$$\Delta S_{\mathrm{conf}} = -R \sum_{i=1}^{n} x_i \ln x_i \quad (1)$$

$$\Delta S_{\mathrm{K-HEHCF}} = -R(0.17\ln 0.17 + 0.21\ln 0.21 + 0.2\ln 0.2 + 0.22\ln 0.22 + 0.2\ln 0.2) = 1.61R$$

$$\Delta S_{\mathrm{Na-HEHCF}} = -R(0.17\ln 0.17 + 0.24\ln 0.24 + 0.22\ln 0.22 + 0.18\ln 0.18 + 0.19\ln 0.19) = 1.60R$$

$\Delta S_{\mathrm{K-HEHCF}} > 1.5\mathrm{R}$, $\Delta S_{\mathrm{Na-HEHCF}} > 1.5\mathrm{R}$.

Supplementary Table 2 Detailed structural information on the K-HEHCF.

K-HEHCF. S.G. Fm-3m. a=b=c=10.0063Å, α=β=γ=90°, Rp=4.96% and Rwp=3.61%.					
Atom	x	y	z	Occupation	Site
C	0.000000	0.000000	0.29448	1.000	24e
N	0.000000	0.000000	0.18353	1.000	24e
K	0.250000	0.250000	0.250000	1.000	8c
Fe2	0.000000	0.000000	0.500000	1.000	4b
Fe1	0.000000	0.000000	0.000000	0.201	4a
Mn	0.000000	0.000000	0.000000	0.210	4a
Co	0.000000	0.000000	0.000000	0.199	4a
Ni	0.000000	0.000000	0.000000	0.202	4a
Cu	0.000000	0.000000	0.000000	0.188	4a

Supplementary Table 3 Detailed structural information on the K-MnHCF.

K-MnHCF. S.G. P21/n. a=10.10970, b=7.32090, c=6.98230Å, α=γ=90.0000°, β=90.2980°, Rp=4.58% and Rwp=5.88%.					
Atom	x	y	z	Occupation	Site
C1	0.005000	0.303000	0.323000	1.000	4e
C2	0.183000	0.517000	0.523000	1.000	4e
C3	0.003400	0.683800	0.298900	1.000	4e
N1	0.004800	0.198400	0.197000	1.000	4e
N2	0.302200	0.504000	0.502200	1.000	4e
N3	0.003000	0.806300	0.209000	1.000	4e
K	0.245120	0.588130	0.061250	1.000	4e
Fe	0.000000	0.500000	0.500000	1.000	2d
Mn	0.000000	0.000000	0.000000	1.000	2a

Supplementary Table 4 EXAFS fitting parameters at the Fe K-edge for various samples (S_0^2=0.72 from Fe-foil).

	shell	CN[a]	R[b](Å)	σ[2c](Å^2)	ΔE$_0$[d](eV)	R factor
Fe-foil	Fe-Fe1	8	2.47±0.01	0.0048	5.8±2.5	0.0037
	Fe-Fe2	6	2.85±0.01	0.0054		
K-HEHCF	Fe-O/N	4.4±0.4	1.84±0.02	0.066	-4.1±2.0	0.0101
	Fe-Fe	7.6±0.9	2.82±0.02	0.0140		

[a]*CN*: coordination numbers; [b]*R*: bond distance; [c]σ^2: Debye-Waller factors; [d] ΔE_0: the inner potential correction. R factor: goodness of fit. Error bounds that characterize the structural parameters obtained by EXAFS spectroscopy were estimated as CN±20%; R ± 1%; σ^2 ± 20%.

Supplementary Table 5 EXAFS fitting parameters at the Mn K-edge for various samples (S_0^2=0.74 from Mn-foil).

	shell	CN[a]	R[b](Å)	σ[2c](Å^2)	ΔE$_0$[d](eV)	R factor
Mn-foil	Mn-Mn	12	2.67±0.01	0.0072	7.9±2.1	0.0163
K-HEHCF	Mn-O/N	3.7±0.2	2.04±0.02	0.0033	-1.4±0.7	0.0171
	Mn-Mn	7.8±0.9	3.05±0.02	0.0215		

[a]*CN*: coordination numbers; [b]*R*: bond distance; [c]σ^2: Debye-Waller factors; [d] ΔE_0: the inner potential correction. R factor: goodness of fit. Error bounds that characterize the structural parameters obtained by EXAFS spectroscopy were estimated as CN±20%; R ± 1%; σ^2 ± 20%.

Supplementary Table 6 EXAFS fitting parameters at the Co K-edge for various samples (S_0^2=0.80 from Co-foil).

	shell	CN[a]	R[b](Å)	σ²[c](Å²)	ΔE₀[d](eV)	R factor
Co-foil	Co-Co	12	2.49±0.01	0.0063	6.8±0.3	0.0011
K-HEHCF	Co-O	2.7±0.3	2.09±0.02	0.0020	4.3±0.7	0.0157
	Co-Co	4.3±0.8	2.95±0.02	0.0200		

[a]*CN*: coordination numbers; [b]*R*: bond distance; [c]σ^2: Debye-Waller factors; [d] ΔE_0: the inner potential correction. R factor: goodness of fit. Error bounds that characterize the structural parameters obtained by EXAFS spectroscopy were estimated as CN±20%; R ± 1%; σ^2 ± 20%.

Supplementary Table 7 EXAFS fitting parameters at the Ni K-edge for various samples (S_0^2=0.82 from Ni-foil).

	shell	CN[a]	R[b](Å)	σ²[c](Å²)	ΔE₀[d](eV)	R factor
Ni-foil	Ni-Ni	12	2.48±0.01	0.0063	6.7±0.9	0.0062
K-HEHCF	Ni-O/N	3.9±0.3	2.04±0.02	0.0030	-2.2±1.0	0.0175
	Ni-Ni	4.5±0.8	2.98±0.02	0.0200		

[a]*CN*: coordination numbers; [b]*R*: bond distance; [c]σ^2: Debye-Waller factors; [d] ΔE_0: the inner potential correction. R factor: goodness of fit. Error bounds that characterize the structural parameters obtained by EXAFS spectroscopy were estimated as CN±20%; R ± 1%; σ^2 ± 20%.

Supplementary Table 8 EXAFS fitting parameters at the Cu K-edge for various samples (S_0^2=0.90 from Cu-foil).

	shell	CN[a]	R[b](Å)	σ^{2c}(Å^2)	ΔE_0[d](eV)	R factor
Cu-foil	Cu-Cu	12	2.54±0.01	0.0086	4.2±0.5	0.0037
K-HEHCF	Cu-O/N	3.4±0.3	2.03±0.02	0.0105	7.1±0.8	0.0194
	Cu-Cu	3.2±0.7	2.89±0.02	0.0160		

[a]*CN*: coordination numbers; [b]*R*: bond distance; [c]σ^2: Debye-Waller factors; [d] ΔE_0: the inner potential correction. R factor: goodness of fit. Error bounds that characterize the structural parameters obtained by EXAFS spectroscopy were estimated as CN±20%; R ± 1%; σ^2 ± 20%.

Supplementary Table 9 Detailed structural information on the Na-HEHCF.

Na-HEHCF. S.G. Fm-3m. a=b=c=10.2890Å, α=β=γ=90°, Rp=4.46% and Rwp=3.16%.					
Atom	x	y	z	Occupation	Site
C	0.000000	0.000000	0.297430	1.000	24e
N	0.000000	0.000000	0.182270	1.000	24e
Na	0.250000	0.250000	0.250000	1.000	8c
Fe2	0.000000	0.000000	0.500000	1.000	4b
Fe1	0.000000	0.000000	0.000000	0.211	4a
Mn	0.000000	0.000000	0.000000	0.201	4a
Co	0.000000	0.000000	0.000000	0.197	4a
Ni	0.000000	0.000000	0.000000	0.198	4a
Cu	0.000000	0.000000	0.000000	0.192	4a

Supplementary Table 10 Detailed structural information on the Na-MnHCF.

Na-MnHCF. S.G. P21/n. a=10.54600, b=7.48200, c=7.42500Å, α=γ=90.0000°, β=92.1020°, Rp=5.14% and Rwp=6.90%.					
Atom	x	y	z	Occupation	Site
C1	0.005000	0.303300	0.322900	1.000	4e
C2	0.183100	0.516900	0.522900	1.000	4e
C3	0.003420	0.683970	0.299100	1.000	4e
N1	0.004810	0.199000	0.196100	1.000	4e
N2	0.302100	0.503800	0.502300	1.000	4e
N3	0.003030	0.806400	0.209000	1.000	4e
Na	0.245230	0.588810	0.061340	1.000	4e
Fe	0.000000	0.500000	0.500000	1.000	2d
Mn	0.000000	0.000000	0.000000	1.000	2a

Supplementary Table 11 Element content of Samples in NaCl solution after cycling (ppm).

Element / Sample	Fe	Mn	Co	Ni	Cu	K
K-HEHCF	0.02	0.17	0.01	0.01	0	0.05

Supplementary Table 12 The comparison of the desalination performance of K-HEHCF with those of the reported materials.

Materials	Voltage/V	NaCl /mg L^{-1}	Adsorption capacity /mg g^{-1}	Cycle number	Capacity retention /%	Ref.
Nb_2CT_x/Nb_2O_5-rGO	1.2	500	41.07	50	81	[7]
SnS_2@NC	1.2	500	49.86	20	87.32	[8]
MCO-NR	1.2	500	33.31	25	90	[9]
$MnCo_2S_4$/g-C_3N_4	1.2	500	71.64	100	92	[10]
CoHCF/PANI	1.4	500	30.48	50	98.1	[11]
CuCoFe-PBA NFs	1.4	500	46.8	100	98	[12]
Ni-PBA/ZC	1.2	500	33.5	50	75	[13]
NiHCF/MXene	1.2	500	26.3	30	84	[14]
MoS_2/S,N-pC	1.4	750	47.9	20	96.7	[15]
$MoSe_2$/MCHS	1.2	500	45.25	10	98	[16]
MnO_2/RGO	1.2	500	52	10	97	[17]
$MnCo_2O_4$@CNFs	1.2	500	34.68	20	90.16	[18]
WS_2@MXene	1.2	500	39.1	40	94.9	[19]
MXene/CuHCF	1.4	500	69.2	50	94.2	[20]
GC/MXene	1.2	500	54.2	30	90	[21]
SCNF@PAMX	1.2	500	31.24	50	78	[22]
K-HEHCF	1.4	500	104.92	200	98	This work

Supplementary references

1. Dai J, *et al.* High-Voltage Potassium Hexacyanoferrate Cathode via High-Entropy and Potassium Incorporation for Stable Sodium-Ion Batteries. *ACS Nano* **17**, 20949-20961 (2023).

2. Zhang H, *et al.* Prussian Blue Analogues with Optimized Crystal Plane Orientation and Low Crystal Defects toward 450 Wh kg−1 Alkali - Ion Batteries. *Angewandte Chemie International Edition* **62**, e202303953 (2023).

3. Wang Y, *et al.* Ultralong Lifespan Zero-Cobalt/Nickel Prussian Blue Analogs Cathode Realized by Solid Solution Reaction Sodium Storage Mechanism. *Advanced Functional Materials* **34**, 2406809 (2024).

4. Wang Y, Liu J, Jiang N, Yang J, Yang C, Liu Y. Highly Crystalline Multivariate Prussian Blue Analogs via Equilibrium Chelation Strategy for Stable and Fast Charging Sodium-Ion Batteries. *Small* **20**, 2403211 (2024).

5. Liu J, Liu J, Tang M, Fu J, Kuang X, Ma J. Boosting Sodium Storage in Prussian Blue Analogs Through Iron Vacancies and Copper Doping. *Advanced Functional Materials* **34**, 2314167 (2024).

6. Zhao B, Wang Y, Wang Z, Hu Y, Zhang J, Bai X. Rational design of Core-Shell heterostructured CoFe@NiFe Prussian blue analogues for efficient capacitive deionization. *Chemical Engineering Journal* **487**, 150437 (2024).

7. Chen Z, Xu X, Wang K, Meng F, Lu T, Pan L. Dual-confinement effect in metal oxide nanoparticles/MXene-reduced graphene oxide for high capacitive deionization performance. *Desalination* **564**, 116733 (2023).

8. Gao M, Liang W, Yang Z, Ao T, Chen W. Flexible ultrathin Nitrogen-Doped carbon mediates the surface charge redistribution of a hierarchical tin disulfide nanoflake electrode for efficient capacitive deionization. *Journal of Colloid and Interface Science* **650**, 1244-1252 (2023).

9. Xu Y, *et al.* Dual redox centers in MnCo2O4 nanorod cathode for highly efficient capacitive deionization. *Desalination* **592**, 118137 (2024).

10. Xu Y, *et al.* High-capacity and high-stability capacitive desalination with dual redox-active MnCo2S4/g-C3N4 heterojunction electrode. *Separation and Purification Technology* **355**, 129761 (2025).

11. Ma D, *et al.* Improved Na+ adsorption performance and storage mechanism of cobalt hexacyanoferrate/polyaniline composite during the hybrid capacitive deionization

process. *Separation and Purification Technology* **348**, 127804 (2024).

12. Guo Y*, et al.* Evolution of CuCoFe Prussian blue analogues with open nanoframe architectures for enhanced capacitive deionization. *Chemical Engineering Journal* **495**, 153714 (2024).

13. Meng F, Ding Z, Xu X, Liu Y, Lu T, Pan L. Metal organic framework-derived nitrogen-doped porous carbon sustained Prussian blue analogues for efficient and fast hybrid capacitive deionization. *Separation and Purification Technology* **317**, 123899 (2023).

14. Chen Z*, et al.* Three-dimensional charge transfer pathway in close-packed nickel hexacyanoferrateΓêÊonΓêÊMXene nano-stacking for high-performance capacitive deionization. *Chemical Engineering Journal* **452**, 139451 (2023).

15. Sharifpour H, Hekmat F, Shahrokhian S. Unraveling the Ion Uptake Capacitive Deionization of Sea- and Highly Saline-Water by Sulfur and Nitrogen Co-Doped Porous Carbon Modified with Molybdenum Sulfide. *ACS Applied Materials & Interfaces* **15**, 42568-42584 (2023).

16. Du J, Xing W, Yu J, Feng J, Tang L, Tang W. Synergistic effect of intercalation and EDLC electrosorption of 2D/3D interconnected architectures to boost capacitive deionization for water desalination via MoSe2/mesoporous carbon hollow spheres. *Water Research* **235**, 119831 (2023).

17. Ahmed F*, et al.* Manganese dioxide nanoparticles/reduced graphene oxide nanocomposites for hybrid capacitive desalination. *Advanced Composites and Hybrid Materials* **6**, 19 (2022).

18. Gao M*, et al.* Encapsulation hierarchical bimetallic oxide with flexible electrospinning carbon nanofibers for efficient capacitive deionization. *Desalination* **586**, 117905 (2024).

19. Zhang S, Fang R, Zhang L, Huang S, Zhao Y, Wang Y. Fully coated WS2 antioxidant film with mesoporous structure for enhancing the structural stability and CDI performance of Mxene. *Desalination* **574**, 117226 (2024).

20. Wang S, Li Z, Wang G, Wang Y, Ling Z, Li C. Freestanding Ti3C2Tx MXene/Prussian Blue Analogues Films with Superior Ion Uptake for Efficient Capacitive Deionization by a Dual Pseudocapacitance Effect. *ACS Nano* **16**, 1239-1249 (2022).

21. Liu Z, Wang Y, Zhou Y, Lee Smith R, Qi X. Confined interfacial self-assembly of graphene-like carbon/MXene composite electrodes for capacitive deionization. *Chemical Engineering Journal* **498**, 155717 (2024).

22. Cheng F, Wang Y, Cai C, Fu Y. Multiscale MXene Engineering for Enhanced Capacitive

Deionization via Adaptive Surface Charge Tailoring. *Nano Letters* **24**, 9477–9486 (2024).